Non-bandgap defect modes in the photoresponse of mid-IR photonic crystal detectors

Non-bandgap defect modes in the photoresponse of mid-IR photonic crystal detectors

M Nobile[1]**, S Schartner**[1]**, W Schrenk**[1]**, A M Andrews**[1]**, P Klang**[1]**, G Strasser**[1,2]**, R Meisels**[3] **and F Kuchar**[3]

[1] Center for Micro- and Nanostructures, Vienna University of Technology, Floragasse 7, 1040 Vienna, Austria
[2] Department of Electrical Engineering and Department of Physics, University at Buffalo, The State University of New York, 332 Bonner Hall, Buffalo, NY 14260-1920, USA
[3] Department of Physics, University of Leoben, Franz Josef Straße 18, A-8700 Leoben, Austria

E-mail: michele.nobile@tuwien.ac.at

Abstract
Non-bandgap defect modes, defect modes showing up in photonic crystal (PhC) structures which do not exhibit a complete photonic bandgap, are investigated experimentally by means of a QWIP (quantum well intersubband photodetector) incorporated within a two-dimensional (2D) triangular photonic crystal of air holes. The modes appear as a local enhancement in the photocurrent spectrum due to an increased in-coupling of surface incident light when a defect mode is present. Such delocalized non-bandgap defect modes and the influence of the entire PhC on their energetic positions are experimentally determined and show good agreement with (2D as well as three-dimensional (3D)) simulations.

(Some figures in this article are in colour only in the electronic version)

1. Introduction

Photonic crystals (PhCs) [1], structures showing a periodic modulation of the dielectric permittivity along one or more directions, have a primary role in today's photonic devices. In particular, two-dimensional (2D) arrangements have been widely employed in many optical devices such as photonic circuits [2–4], fibers [5], and lasers [6–10]. In the particular case of intersubband based devices, PhCs are very attractive because they allow the in- and out-coupling of light via the surface, coupling which would not be directly achievable due to the transverse magnetic (TM)-polarized nature of intersubband emitted/detected light. PhCs used as a coupling mechanism, where mainly shallow gratings have been utilized either for detection [11] or emission [12, 13], could have advantages in terms of increased cavity design freedom, the possibility of surface emission, and the compactness of the device itself. This has already been shown by a surface emitting PhC quantum cascade lasers (QCL) [10].

Also in terms of intersubband or intersublevel based detectors such as QWIPs or quantum dot infrared photodetectors (QDIPs) one can take advantage of a PhC cavity [14]. In the case of a PhC detector one can use this device also as a characterization tool for PhCs.

The coupling between an incoming light wave and the PhC structure gives rise to the possibility of an accurate mapping of the photonic band structure, as shown in [15]. In this case a GaAs/AlGaAs QWIP was incorporated within a surface-plasmon/plasmon-enhanced structure [16, 17] and a triangular array of air holes was etched into it. By illuminating the devices via their surface at different incident angles, the light is coupled into the structure whenever the in-plane wavevector and the energy of the incoming light wave match a point of the photonic band structure. The TM-polarized excited modes can thus be absorbed by the QWIP, causing peaks to appear in the photocurrent spectrum. Each peak can be identified with a particular PhC mode, similarly to the features observed in reflectivity measurements of the PhCs reported by Astratov *et al* [18]. This technique is of course not only restricted to
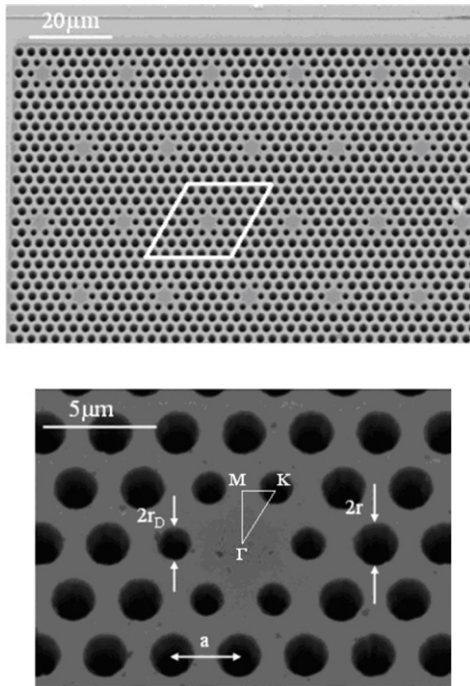
1

Figure 1. SEM pictures of a finished device. The white parallelogram highlights the unit cell of the 7×7 defect arrangement (top figure). This unit cell was also used for 2D simulations of the defect mode. In the bottom figure, a close up of the defect structure shows the relevant dimensions a, r and r_D. The defect consists of a single missing hole with the six nearest neighbors being varied in diameter. The lattice period a is 3 μm.

Figure 2. Calculated photonic band structure of a triangular lattice for TM polarization and two different values of r/a. The lattice period is 3 μm and the effective index of the material is 3.2.

the investigation of band-edge modes, it can also be extended to characterize defect states [15] as well. Such defect modes are especially interesting for compact emitting structures [6] since they allow for extremely small modal volumes.

This work is concerned with non-bandgap defect modes, defect modes appearing in PhC structures which do not show a complete bandgap for the light in the polarization of interest. We will show how the frequency of such modes can be experimentally determined and, since non-bandgap defect modes are more delocalized compared to bandgap modes [19], how the mode frequency is tuned by changing the geometrical parameters of the PhC.

2. Device description

2.1. Photonic crystal and defects

In figure 1, SEM (scanning electron microscopy) pictures of fabricated samples are presented. They consist of a mesa structure in which a triangular lattice of holes was etched. A calculated TM band structure is shown in figure 2 for two different hole sizes. It is only the TM band structure which is of importance for this type of devices since the detection is restricted to TM-polarized light only. In this case no photonic bandgap is present.

Single missing hole defects were introduced and the size of the six holes surrounding the defect (defect holes) was modified. This makes tuning of the defect mode frequency
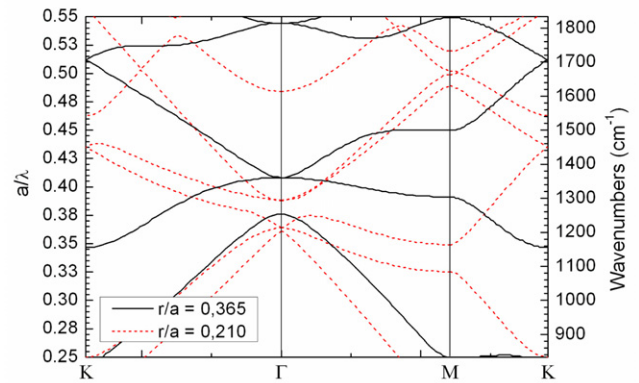
possible. Devices with different r/a and r_D/r have been processed, where a, r, and r_D are the lattice period, the radius of the normal holes, and the radius of the defect holes respectively (figure 1). The lattice period is always kept at a value of 3 μm. The above mentioned defect structure was repeated with a period of $7a$, resulting in a 7×7 supercell structure. In addition, for each type of defect structure defect-free reference structures were fabricated to ensure the origin of the defect related photocurrent peaks.

In order to make defect modes visible in the photocurrent spectra, the design was slightly modified in comparison to that presented in [15]. In this former publication no defect modes could be observed, most probably due to the small r/a value ($r/a = 0.21$) used.

As can be seen in figure 2, the second and the third crossings at the Γ-point (dotted lines) are very close to each other for $r/a = 0.21$. This prevents the observation of defect modes in this frequency range because the linewidths of the observed peaks is broader than the separation between them. Thus the corresponding peaks will overlap, giving rise to a single broad feature and aggravating a clear assignment. By increasing r/a, the spacing between the bands increases (solid lines in figure 2). This leads to a larger separation between the modes and consequently to more distinguishable peaks in the photocurrent spectra.

2.2. Waveguide

The vertical structure of the device consists of the quantum well/barrier structure forming the QWIP (described in section 3.1), placed within a surface-plasmon [16]/plasmon-enhanced [17] waveguide. A profile of the fundamental TM mode is reported in figure 3. The surface-plasmon cladding realized via the top contact allows a thin waveguide with a high confinement of the optical mode within the detecting region. This is, however, compromised by higher losses originating from the metal film. The reduced waveguide thickness significantly eases the deep etching process since the PhC holes need to be etched through the whole waveguide structure in order to ensure its guiding ability. The lower cladding is
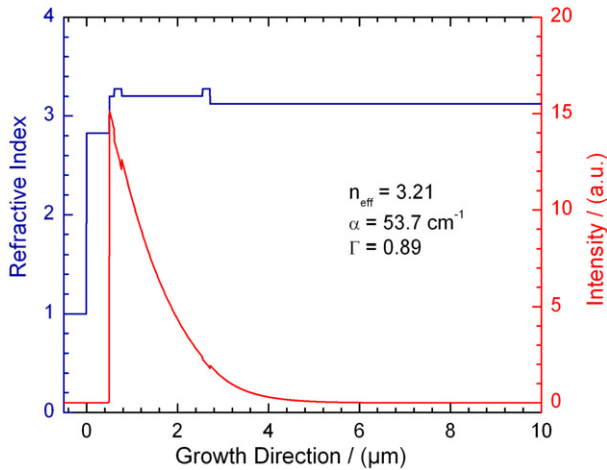
Figure 3. Profile of the fundamental TM mode of the waveguiding structure calculated for a wavenumber of 1667 cm^{-1}.
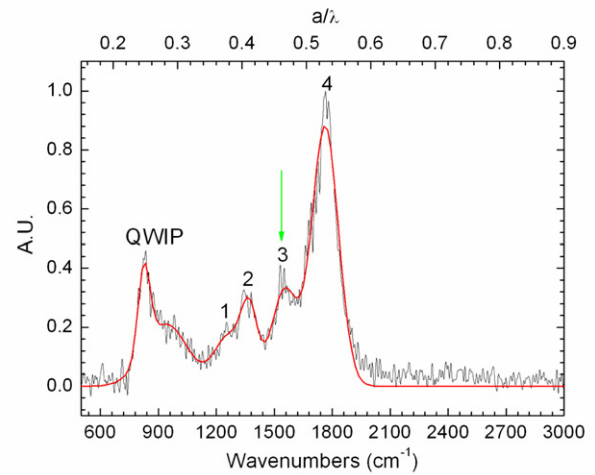

Figure 4. Photocurrent spectrum of a device with $r/a = 0.365$ and $r_D/r = 0.777$. The arrow highlights the peak corresponding to the defect mode.

formed by a highly doped GaAs layer and the highly doped substrate (both 2×10^{18} cm^{-3}). The high doping shifts the plasma frequency towards the mid-IR region, lowering the refractive index of GaAs. At a wavenumber of 1667 cm^{-1}— which corresponds to the spectral region where most PhC measurements have been performed—our simulations yield an effective refractive index of 3.2 for the fundamental TM mode. This index was then used in the 2D plane wave expansion method (PWEM) simulations [20] to calculate the photonic band structure and the defect modes.

3. Fabrication

3.1. Growth

The detecting region is made up of 50 periods of a standard GaAs/Al$_{0.19}$Ga$_{0.81}$As bound-to-quasibound QWIP [21] and was grown by molecular beam epitaxy. The well and barrier thicknesses are $w = 6.6$ nm and $b = 54$ nm respectively. The wells are delta doped to an equivalent sheet density of 3×10^{11} cm^{-2}. Starting from the highly doped (2×10^{18} cm^{-3}) substrate, the layer sequence is as follows: 540 nm GaAs (2×10^{18} cm^{-3}) acts as a lower cladding followed by an undoped 216 nm Al$_{0.19}$Ga$_{0.81}$As spacer layer and the detecting region (2.796 μm). Subsequently another 216 nm Al$_{0.19}$Ga$_{0.81}$As spacer layer (undoped) was grown before the contact facilitating layers: 108 nm GaAs (1×10^{18} cm^{-3}) and 5 nm In$_{0.53}$Ga$_{0.47}$As (1×10^{19} cm^{-3}). All layer thicknesses and Al contents were confirmed from x-ray diffraction measurements after growth.

3.2. Device processing

A Ge/Au/Ni/Au (15/30/14/60 nm) top contact layer was first evaporated on the sample, followed by the deposition of a 300 nm-thick SiN$_x$ layer. After that a 250 nm-thick PMMA layer was spun and patterned by direct e-beam writing. The PhC pattern was then transferred via SF$_6$ reactive ion etching (RIE) into the SiN$_x$ layer. The patterned SiN$_x$ serves as a

hard mask for Ar RIE of the top contact, avoiding in this way a metal deposition after the deep etching step which could potentially short circuit the device. After the patterning of the metal top contact, the PhC was deep etched together with the mesa by SiCl$_4$/N$_2$ RIE [22] where hole depths of ∼5.5 μm have been achieved. A SiN$_x$ insulation, Ti/Au contact pads, and a Ge/Au/Ni/Au (15/30/14/60 nm) backside contact finish the processing.

4. Results and discussion

4.1. Measurement setup

The samples were mounted in a liquid He flow cryostat kept at a temperature of 10 K. The PhC devices were illuminated by means of a mid-IR broadband source at surface normal incidence or at specific angles of incidence and under different incoming polarizations. The angular resolution was ±5°, given by a 1 inch diaphragm and a 6 inch parabolic mirror used to focus the light on the sample. The generated photocurrent was spectrally resolved by passing the exciting light through a Fourier transform infrared (FTIR) spectrometer and feeding back the photocurrent into the FTIR. Each peak in the measured photocurrent spectrum refers to the energetic position of a particular mode of the PhC structure.

4.2. Band structure and defect mode mapping

In figure 4, we report the photocurrent spectrum for normal incidence of a device with $r/a = 0.365$ and $r_D/r = 0.777$.

The lowest frequency peak at ∼800 cm^{-1} (including its shoulder) reproduces the spectral responsivity of the QWIP and originates from non-resonant scattering at the small apertures given by the PhC holes. The other features are related to the PhC structure. A deconvolution of these remaining peaks into multiple Lorentzian functions results in four peaks of similar linewidth (∼150 cm^{-1}). Three of them (at 1268, 1377 and 1757 cm^{-1}) are in perfect agreement with 2D
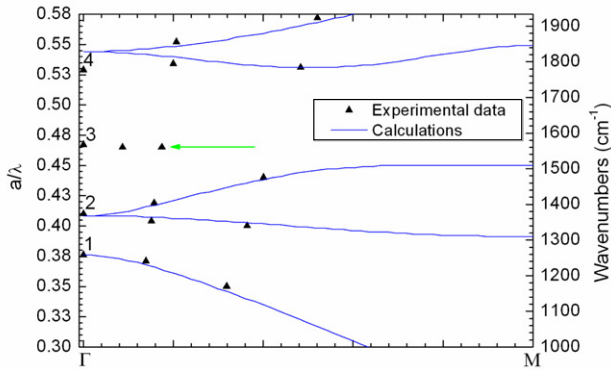
Figure 5. Calculated photonic band structure in the ΓM direction and for TM polarization of a triangular lattice with $r/a = 0.365$. The black triangles correspond to the experimental points taken at different incidence angles and moving along the ΓM direction. The arrow highlights the defect mode branch.

PWEM simulations. Figure 5 shows a mapping of the angular dependence of these peaks together with the band structure calculated for an r/a value of 0.365. This is in good agreement with the value of $r/a = 0.355$ which we deduced from SEM investigations. The main discrepancy between calculated and measured band structure is attributed to arise from not considering dispersion in our PWEM calculations. Dispersion is caused though by both cladding layers of Au and highly doped GaAs due to Drude absorption.

Beside these peaks associated to the modes of the ordinary triangular lattice, a further peak (labeled 3) is clearly visible at a wavenumber of ~1558 cm^{-1} ($a/\lambda \sim 0.467$). Its mapping onto the reduced zone scheme shows no dispersion as expected for defect modes.

In order to assign this additional peak to a distinct defect mode we fabricated a number of devices with different r/a and r_D/a values and compare the frequency shift of the defect related peak to simulations. To this aim, we measured the photocurrent spectrum (normal incidence) of devices whose r_D/r is fixed at a value of 0.757, while the values of r/a change between 0.3 and 0.4. Three spectra out of this series are presented in figure 6(a). Again the aforementioned peak (labeled A1) is clearly visible in all the spectra. The frequency shift is collected in figure 6(b), where also simulation results are given. 2D PWEM calculations are employed again to obtain the mode profiles as well as the resonant frequencies. This time the calculation was carried out using a supercell approach [20] with a supercell size of 7×7. This reproduces the actually fabricated structure. Mode profiles of defect states found in the region of interest are shown in figure 6(c). Out of four modes, a dodecapol (A2), a monopole (A1), and two quadrupoles (E2a and E2b), monopole A1 fits the experimental data best, being in agreement with [23].

Additionally 3D FDTD (finite difference time domain) simulations have been performed. In this way the actual multilayer composition is included as well as the hole depth instead of using an effective index approach as for the PWEM.
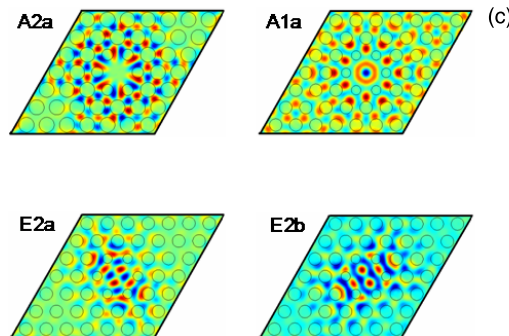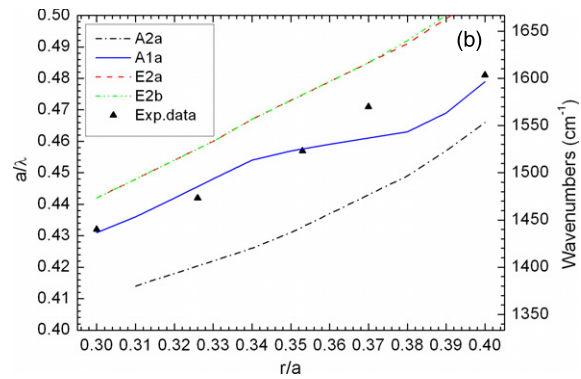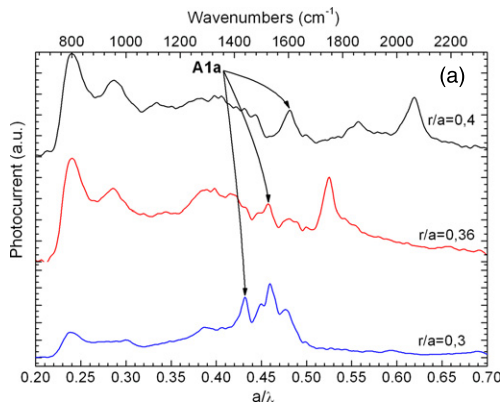

Figure 6. (a) Photocurrent spectra of a device with $r_D/r = 0.757$ for different values of r/a. (b) Calculated reduced frequencies of several defect modes as a function of r/a ($r_D/r = 0.757$). The black triangles correspond to the measurement. (c) Calculated spatial distribution of the out-of-plane electric field of the defect modes in (b).
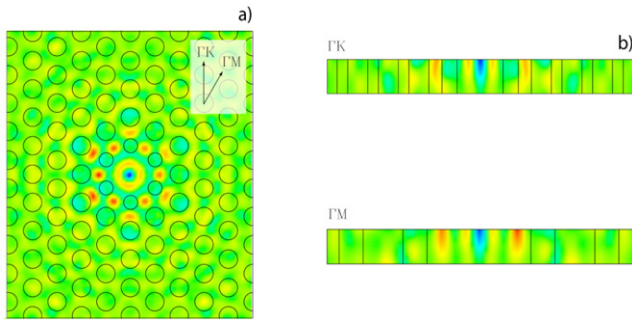
Figure 7. Cross section of the electric field distribution for the component normal to the surface obtained from 3D FDTD simulations. (a) Top view of the field distribution of the defect mode at $a/\lambda = 0.435$ ($r/a = 0.326$, $r_D/r = 0.757$). (b) Sections of the mode profile along ΓK and ΓM directions, which highlight the distribution of the defect mode within the active layers of the detector.

Figure 8. Defect mode frequency as a function of supercell size in the case of the monopole-like profile A1a ($r/a = 0.365$, $r_D/r = 0.7$).

For values $r/a = 0.326$ and $r_D/r = 0.757$ the defect mode is found at $a/\lambda = 0.435$, in good agreement with 2D PWEM simulations which yield $a/\lambda = 0.44$. In figure 7 mode profiles (electric field component in the vertical direction) are presented for different cross sections. Figure 7(a) shows a top view where the actual cut-plane is placed on top of the active region directly below the metallic layer. A comparison with the mode profile in figure 6(c) shows that both are of the same symmetry (irreducible representation A1) and have an identical number of radial nodes. Cross sections along ΓK and ΓM for planes normal to the surface are shown in figure 7(b). The vertical profiles exhibit typical surface-plasmon modes, being strongly attached to the metallic layer on top.

The improvement in linewidth compared to the samples presented in figure 4 is most likely due to a changeover in fabrication processes from standard UV contact lithography to electron beam lithography. We attribute linewidth mainly to imperfections caused by the manufacturing process as will be discussed in the following. The hole diameters are not homogeneous throughout the device and an examination via SEM pictures reveals a variance in hole diameter of $\pm 1.5\%$ (± 16.4 nm). This small variation is connected with a variation of the resonant frequencies. From a linear fit to the experimentally found defect frequencies we deduce a relative frequency shift over r/a that calculates a variance of around ± 26 cm^{-1} for the mentioned variation of $\pm 1.5\%$ in r/a. This is in reasonable agreement with the experimental data ($\Delta\nu \approx 20$–35 cm^{-1}). Similar considerations apply for the band-edge modes.

4.3. Delocalization of non-bandgap defect modes

As already mentioned, we are dealing with a PhC structure that does not have a bandgap for TM polarization. The bandgap for transverse electric (TE) light cannot be exploited since the detecting region of a QWIP is insensitive to TE-polarized light. Although there is a lack of a photonic bandgap for the TM light, the defects still support localized states as the experiments show. In particular, the non-dispersive behavior is
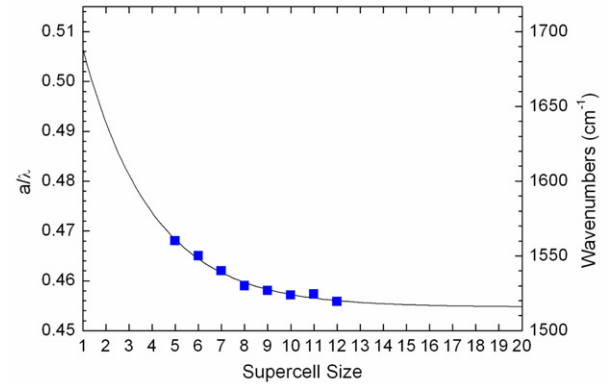
a strong indication of a localized mode since localization in real space implies delocalization in k-space. However, compared to defect states as they appear within a photonic bandgap, the non-bandgap defect states supported in our structure are expected to be more extended over the whole unit cell instead of being highly localized at the defect [19]. This can already be seen in figure 6(c) where defect modes are represented by the electric field profiles. As a result of this poorer localization, the coupling between neighboring defects is enhanced even for relatively large supercells and the corresponding resonant frequencies are therefore shifted. In order to gain an insight into the reach of this coupling, we calculate the frequency change of the mode A1 for different supercell sizes. The results are presented in figure 8.

As can be seen, the frequency of the defect mode converges to a value which can be considered as the isolated defect frequency only for relatively large supercells of around 20×20, whereas for simulations with bandgap defect modes a typical supercell size of 5×5 is sufficient [20].

5. Summary

An investigation into non-bandgap defect modes in a triangular lattice PhC has been performed by means of a QWIP detecting region incorporated within the material. The photocurrent spectra of devices with defects show very clear additional peaks, which allow the frequencies of the defect modes to be experimentally determined. By comparison with calculations, one defect mode with a monopole-like profile is identified in our case. The frequency of such a mode is found to depend on r/a and this is basically due to the lack of a full TM gap which causes the defect modes to be delocalized.

References

[1] Joannopoulos J D, Villeneuve P R and Shanhui F 1997 Photonic crystals *Nature* **386** 165–73

[2] Tanaka Y, Sugimoto Y, Ikeda N, Nakamura H, Kanamoto K, Asakawa K and Inoue K 2005 Design, fabrication, and characterization of a two-dimensional photonic-crystal symmetric Mach–Zehnder interferometer for optical integrated circuits *Appl. Phys. Lett.* **86** 141104

[3] Busch K, Lölkes S, Wehrspohn R B and Föll H 2004 *Photonic Crystals* (Weinheim: Wiley–VCH)

[4] Viasnoff-Schwoob E, Weisbuch C, Benisty H, Cuisin C, Derouin E, Drisse O, Duan G H, Legouezigou L, Zegouezigou O, Pommereau F, Golka S, Heidrich H, Hensel H J and Janiak K 2005 Compact wavelength monitoring by lateral outcoupling in wedged photonic crystal multimode waveguides *Appl. Phys. Lett.* **86** 101107

[5] Russell P 2003 Photonic crystal fibers *Science* **299** 358–62

[6] Painter O, Lee R K, Scherer A, Yariv A, O'Brien J D, Dapkus P D and Kim I 1999 Two-dimensional photonic band-gap defect-mode laser *Science* **284** 1819–21

[7] Park H G, Kim S H, Kwon S H, Ju Y G, Yang J K, Baek J H, Kim S B and Lee Y H 2004 Electrically driven single-cell photonic crystal laser *Science* **305** 1444–7

[8] Happ T D, Kamp M, Forchel A, Gentner J L and Goldstein L 2003 Two-dimensional photonic crystal coupled-defect laser diode *Appl. Phys. Lett.* **82** 4–6

[9] Wu X, Yamilov A, Liu X, Li S, Dravid V P, Chang R P H and Cao H 2004 Ultraviolet photonic crystal laser *Appl. Phys. Lett.* **85** 3657–9

[10] Colombelli R, Srinivasan K, Troccoli M, Painter O, Gmachl C, Tennant D M, Sergent A M, Sivco D I, Cho A Y and Capasso F 2003 Quantum cascade surface-emitting photonic crystal laser *Science* **302** 1374–7

[11] Andersson J Y and Lundquist L 1991 Near-unity quantum efficiency of AIGaAs/GaAs quantum well infrared detectors using a waveguide with a doubly periodic grating coupler *Appl. Phys. Lett.* **59** 857–9

[12] Hofstetter D, Faist J, Beck M and Oesterle U 1999 Surface-emitting 10.1 μm quantum-cascade distributed feedback lasers *Appl. Phys. Lett.* **75** 3769–71

[13] Schrenk W, Finger N, Gianordoli S, Hvozdara L, Strasser G and Gornik E 2000 Surface-emitting distributed feedback quantum-cascade lasers *Appl. Phys. Lett.* **77** 2086–8

[14] Posani K T, Tripathi V, Annamalai S, Weisse-Bernstein N R, Krishna S, Perahia R, Crisafulli O and Painter O J 2006 Nanoscale quantum dot infrared sensors with photonic crystal cavity *Appl. Phys. Lett.* **88** 151104

[15] Schartner S, Golka S, Pflügl C, Schrenk W, Andrews A M, Roch T and Strasser G 2006 Band structure mapping in photonic crystal intersubband detectors *Appl. Phys. Lett.* **89** 151107

[16] Sirtori C, Gmachl C, Capasso F, Faist J, Sivco D I, Hutchinson A L and Cho A Y 1998 Long-wavelength ($\lambda \approx 8$–11.5 μm) semiconductor lasers with waveguides based on surface plasmons *Opt. Lett.* **23** 1366–8

[17] Sirtori C, Kruck P, Barbieri S, Page H, Nagle J, Beck M, Faist J and Oesterle U 1999 Low-loss Al-free waveguides for unipolar semiconductor lasers *Appl. Phys. Lett.* **75** 3911–3

[18] Astratov V N, Whittaker D M, Culshaw I S, Stevenson R M, Skolnick M S, Krauss T F and De-La-Rue R M 1999 Photonic band-structure effects in the reflectivity of periodically patterned waveguides *Phys. Rev.* B **60** R16255–8

[19] Sakoda K 2001 *Optical Properties of Photonic Crystals* vol 80 (Berlin: Springer)

[20] Guo S and Albin S 2003 A simple plane wave implementation method for photonic crystal calculations *Opt. Express* **11** 167–75

[21] Schneider H and Liu H C 2007 *Quantum Well Infrared Photodetectors* vol 126 (Berlin: Springer)

[22] Golka S, Schartner S, Schrenk W and Strasser G 2007 Low bias reactive ion etching of GaAs with a $SiCl_4/N_2/O_2$ time-multiplexed process *J. Vac. Sci. Technol.* B **25** 839–44

[23] Schartner S, Nobile M, Schrenk W, Andrews A M, Klang P and Strasser G 2008 Photocurrent response from photonic crystal defect modes *Opt. Express* **11** 4797–803